




Nanoscale viscosity of confined polyethylene oxide

Zheng Zhang,¹ Junjun Ding ², Benjamin M. Ocko,³ Andrei Fluerașu,³ Lutz Wiegart,³ Yugang Zhang,³ Mark Kobrak,⁴ Ye Tian,¹ Honghu Zhang,¹ Julien Lhermitte,¹ Chang-Hwan Choi,² Frank T. Fisher ², Kevin G. Yager ^{1,*} and Charles T. Black^{1,†}

¹Center for Functional Nanomaterials, Brookhaven National Laboratory, Upton, New York, USA

²Department of Mechanical Engineering, Stevens Institute of Technology, Hoboken, New Jersey, USA

³National Synchrotron Light Source II, Brookhaven National Laboratory, Upton, New York, USA

⁴Brooklyn College and the Graduate Center of the City University of New York, Brooklyn, New York, USA



(Received 20 August 2019; published 19 December 2019)

Complex fluids near interfaces or confined within nanoscale volumes can exhibit substantial shifts in physical properties compared to bulk, including glass transition temperature, phase separation, and crystallization. Because studies of these effects typically use thin film samples with one dimension of confinement, it is generally unclear how more extreme spatial confinement may influence these properties. In this work, we used x-ray photon correlation spectroscopy and gold nanoprobe to characterize polyethylene oxide confined by nanostructured gratings (<100 nm width) and measured the viscosity in this nanoconfinement regime to be ~ 500 times the bulk viscosity. This enhanced viscosity occurs even when the scale of confinement is several times the polymer's radius of gyration, consistent with previous reports of polymer viscosity near flat interfaces.

DOI: [10.1103/PhysRevE.100.062503](https://doi.org/10.1103/PhysRevE.100.062503)

I. INTRODUCTION

Confinement of molecular and macromolecular species within nanoscale volumes is a useful strategy for designing material properties, since the composite material can exhibit performance exceeding any of the constituents [1]. The enhanced, emergent properties of the composite typically stem from substantial changes in the fundamental behaviors of the confined species. For instance, the crystallization and orientation of semiconducting polymers can be controlled by nanoconfinement [2,3], which in turn influences the material's electronic properties [3,4]. Nanoconfined polymers exhibit properties that deviate substantially from those of the bulk, including local dynamics [5], glass transition [6–8], crystallization [9], shape memory [10,11], capillary instability [12,13], phase separation [14,15], and stiffness [16]. These changes arise from both entropic and enthalpic effects; interfaces restrict the accessible chain conformations [17,18], modify entanglement density [19], and may exhibit preferential chemical affinity [20]. Most studies of the effects of nanoconfinement use ultrathin films as model systems, in which the material is confined in one dimension by substrate and free-surface interfaces, i.e., confined to a two-dimensional (2D) volume. Here we use nanogratings, a comparatively unexplored confining geometry, to study the effect of nanoconfinement. In such cases, the proximity of multiple interfaces may synergistically enhance confinement effects or may compete and nullify any effect.

Although viscosity is a fundamental property of complex fluids, affected by both molecular and collective properties,

there is at present an incomplete understanding of how the rheological response of polymer melts may shift under nanoconfinement; in particular, it is unclear whether the behavior observed for thin films can be extrapolated to confinement along two or even all three spatial dimensions [21,22]. For example, at extremely small scales, confinement can prevent molecular jamming and promote ballistic transport, which greatly lowers effective viscosity [19,23]. However, slightly larger confining volumes instead frustrate molecular motions and increase effective viscosity [24–26]. This knowledge gap is due in part to the challenge of accurately measuring dynamics under nanoconfinement, with respect to both material preparation (fabricating and filling nanovolumes) and measurement (probing ultrasmall volumes).

Here we use coherent x-ray scattering to directly probe the nanoscale viscosity of polymer melts confined in nanogratings. We use gold nanoparticles as tracers, inferring nanoscale rheology from the stochastic motion of the particles. We observe that even at confinement size scales considerably larger than the characteristic polymer chain size (radius of gyration), the measured nanoscale melt viscosity is substantially higher than that observed in the bulk. In particular, for polyethylene oxide (PEO) confined to ~ 100 nm channels, the effective viscosity experienced by nanoparticle tracers is more than two orders of magnitude larger than the bulk PEO viscosity.

II. METHODS

A. Materials

Polyethylene oxide dihydroxy-terminated (PEO30k), $M_w = 39$ kg/mol, $M_w/M_n = 1.18$, was obtained from Polymer Source, Inc., and used as received. Twenty nanometer diameter and 10 nm diameter gold nanoparticles (AuNPs; dispersed in water and stabilized by a trace amount

*kyager@bnl.gov

†ctblack@bnl.gov

of citrate) were obtained from TedPella, Inc. The as-received solutions of 20 nm AuNPs were concentrated to ~ 20 nM by centrifugation before use. Solutions of 10 nm AuNPs were concentrated to ~ 340 nM. Experiments on both particle sizes were performed. Reported nanoconfinement results are based on the smaller particle size to minimize the ratio between particle size and confinement size scale.

B. Fabrication

Fabrication of nanostructured templates started with n-type crystalline Si(100) wafers ($0.001\text{--}0.005\ \Omega\cdot\text{cm}$). MCC Primer 80/20 (MicroChem) was spin coated onto a Si wafer at 7000 rpm as an adhesion promoter. A negative photoresist, NR7-250P (Futurrex, Inc.), was subsequently spin coated at 7000 rpm for 40 s and then placed on a hot plate at 150°C for 1 min, resulting in a thickness of ~ 150 nm. A custom two-degrees-of-freedom Lloyd-mirror interferometer built with a 325 nm wavelength HeCd laser (Model IK3501R-G, Kimmon Koha Co.) was used for exposure [27]. For this experiment, the exposure angle between the sample surface normal and the laser beam was adjusted to 53° , resulting in a periodicity of 270 nm. For nanogratings, a dose of $7\ \text{mJ}/\text{cm}^2$ was used. For nanopore arrays, the exposure was split in two steps [28]: first with a dose of $6\ \text{mJ}/\text{cm}^2$, followed by another $6\ \text{mJ}/\text{cm}^2$ after rotating the wafer by 90° . After exposure, the sample was baked at 100°C for 1 min, developed in diluted RD6 (Futurrex, Inc., 33.3 vol% in deionized water), for 6 s, rinsed in deionized water 30 s, and dried with a nitrogen gun.

The resist pattern was transferred to Si wafers via reactive ion etching on an Oxford Instruments Plasmalab 100 using a two-step process: 40 sccm SF_6 , 18 sccm O_2 , 15 mTorr, -100°C , ICP 800 W, and RF 40 W for 3 s followed by 7 W for 60 s. Remaining resist was stripped using N-methyl-2-pyrrolidone.

The final Si nanostructures were measured by SEM and SAXS to confirm quality. Nanogratings were line-and-space patterns with trenches 91 ± 9 nm width, 953 ± 13 nm depth, and 270 ± 1 nm spacing. The nanopores were square-grid arrays of cylindrical pores with 105 ± 5 nm diameter, 831 ± 15 nm depth, and 270 ± 1 nm repeat spacing.

The patterned Si substrates were cleaned with O_2 plasma on a March etcher (100 mTorr, RF 20 W for 3 min) before filling with polymer. PEO was filled into the nanovolumes by spinning coating from an acetonitrile solution in a humidity-controlled dry room. For PEO/AuNP composites, a mixed solution of concentrated AuNP and PEO solution was used. The concentration of the solution and spinning speed were controlled for optimum filling (no overfilling). The as-cast samples were annealed in vacuum at 85°C (above the melting transition of bulk PEO, $\sim 65^\circ\text{C}$; and well above the glass transition temperature, which is below room temperature) for 1 h to remove residual solvent [29] and facilitate PEO flow into the confining volumes. Samples were sealed in argon-filled polypropylene-lined vacuum pouches before characterization.

We verified the filling amount by imaging the cross-sectional morphology using a Hitachi S-4800 scanning electron microscope. Because PEO has poor cleavability at room temperature, we used sequential infiltration synthesis to convert the PEO into a more brittle inorganic composite (i.e.,

loaded with AlO_x), when preparing SEM cross-sectional samples [30,31].

C. X-ray photon correlation spectroscopy (XPCS)

XPCS measurements were performed at the 11-ID Coherent Hard X-ray (CHX) beamline at National Synchrotron Light Source II (NSLS-II), with a fixed photon energy of 9.65 keV (photon wavelength $\lambda = 1.29\ \text{\AA}$) and a beam size of $10\ \mu\text{m} \times 10\ \mu\text{m}$. Beamline stability was tested on static samples, confirming that one observes a constant signal (no measurable decorrelation) even to timescales of 10^4 s. Samples were mounted on a thermal stage under vacuum. X-ray beam damage effects were probed by measuring decorrelation curves as a function of total x-ray dose and selecting the dose regime where the computed time constant is independent of dose. The total x-ray exposure time was limited to 200 ms (for the full, unattenuated beam) for the presented results. A millisecond shutter and an attenuator system made of double-side polished silicon wafers were used to spread the 200 ms full-beam equivalent dose over the timescales required by the experiment. The unattenuated incident beam flux was measured to be 3×10^{11} photons/s at the sample position. The maximum sample dose can be estimated using this full beam flux and the maximum (200 ms) exposure time. Accounting for the incident angle of 0.24° , the areal photon dose onto the sample was $3 \times 10^6\ \text{ph}/\mu\text{m}^2$, corresponding to an areal energy dose of $4\ \text{nJ}/\mu\text{m}^2$. Of course, only a fraction of this incident radiation is absorbed in the polymer sample.

III. RESULTS AND DISCUSSION

We fabricated nanogratings in silicon substrates (91 nm trench width, 270 nm pitch) using laser interference lithography [27] and dry plasma etching [32] [schematic in Fig. 1(b); see Fig. S1 in the Supplemental Material [33] for top-view scanning electron microscope (SEM) images]. The high-density and wide-area patterning ($20\ \text{mm} \times 20\ \text{mm}$) increased the amount of confined material available for study. We controllably filled these nanogratings with PEO via spin casting, followed by vacuum annealing slightly above the polymer melting temperature ($\sim 65^\circ\text{C}$), which results in nanogratings filled with PEO from the bottom up [Fig. 1(c)]. We optimized these preparation conditions to slightly underfill the confining volumes to ensure no unconfined material remained atop the substrate, so that subsequent measurements probed only confined material (Fig. S2).

In order to measure the viscosity of nanoscale volumes of polymer material, we used x-ray photon correlation spectroscopy (XPCS) at the National Synchrotron Light Source II (NSLS-II, Brookhaven National Lab). This technique illuminates the material of interest with a highly coherent x-ray beam, measuring the decorrelation of the scattering pattern with time [34,35]. This differs from conventional small-angle x-ray scattering (SAXS), which uses a beam with minimal coherence, in which case the far-field scattering pattern arises from interference within individual nano-objects and between nearby nano-objects. With a highly coherent x-ray beam, the pattern contains speckles arising from interobject scattering from all nano-objects within a coherence volume (Fig. 2). The

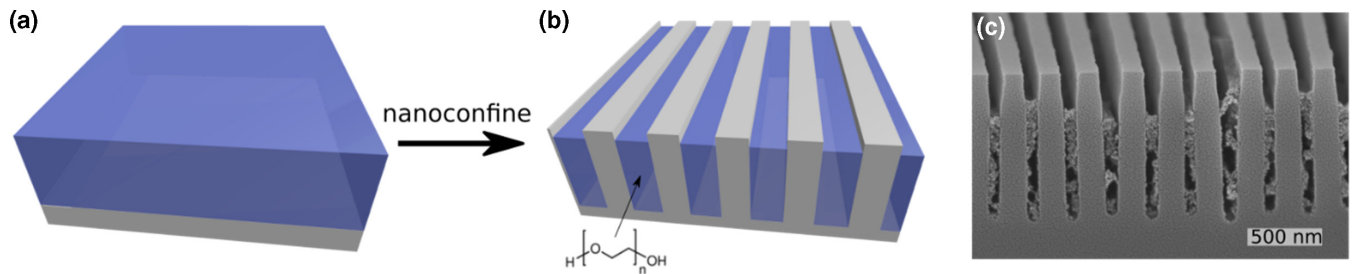


FIG. 1. (a) Schematic bulk and (b) nanograting filled with PEO. (c) SEM image of nanograting filled with PEO. SEM image was taken at 70° sample tilt. A sputtered silver coating was used to reduce charging effects, and the PEO was infiltrated with alumina to improve image contrast.

speckles encode the distance between objects and vary in time if the objects are dynamically moving. The time for a typical speckle to decorrelate is a robust measure of the dynamical properties.

Because of the low scattering contrast of soft materials, the XPCS measurements were carried out in a manner to enhance the signal (Fig. 2). First, we measure the samples in grazing-incidence (GI) geometry, where the x-ray beam reflects off the substrate interface at a glancing angle. This geometry improves the overall scattering intensity, owing to beam projection, making GI-XPCS uniquely suited for studying the dynamics of ultrathin film nanostructures [36]. Previous XPCS measurements of polymer-coated gratings [37] were performed at an incident angle less than the critical angle, in order to measure surface height fluctuations (capillary waves). Such measurements are by design insensitive to the behavior in the polymer well below the surface, which is the focus of our study. We measure using an incident angle above the critical angle in order to probe the entire depth of the film. Second, we disperse gold nanoparticles (AuNPs) at low concentration within the polymer matrix, giving rise to a form factor scattering signal that encodes particle size [35,38,39]. The XPCS measurements of the Brownian motion of these nanoparticle “tracers” is a robust reporter of the

viscosity which the tracers experience [39,40]. The particle-particle scattering produces coherent speckles (see Figs. S3 and S4), which fluctuate as AuNP diffusion through the polymer matrix changes the interparticle distances. The temporal intensity-intensity autocorrelation of these speckles can be used to probe dynamics. Finally, we measure grating-confined material with the x-ray beam orthogonal to the grating grooves (i.e., the q_r direction is along the grooves). In this geometry, the strong structural peaks from the grating—which could overwhelm the scattering from the nanoparticles—do not appear on the detector.

We use a low AuNP concentration (0.09 vol%) to minimize particle agglomeration and to probe the dilute-particle regime. Using electron microscopy, we verified that AuNPs are homogeneously dispersed throughout the PEO and localized within the nanoconfinement volumes [Fig. 2(a), inset]. Importantly, we imaged nanoconfined samples after thermal cycling to verify that AuNPs remain dispersed and do not preferentially migrate and stick to any of the confining volume sidewalls. Nevertheless, it is difficult to eliminate the possibility that a fraction of nanoparticles form dimers or larger aggregates; we discuss below the corresponding implications for data analysis. Because we are interested in probing the full depth of the confining volumes, we selected an x-ray incidence angle

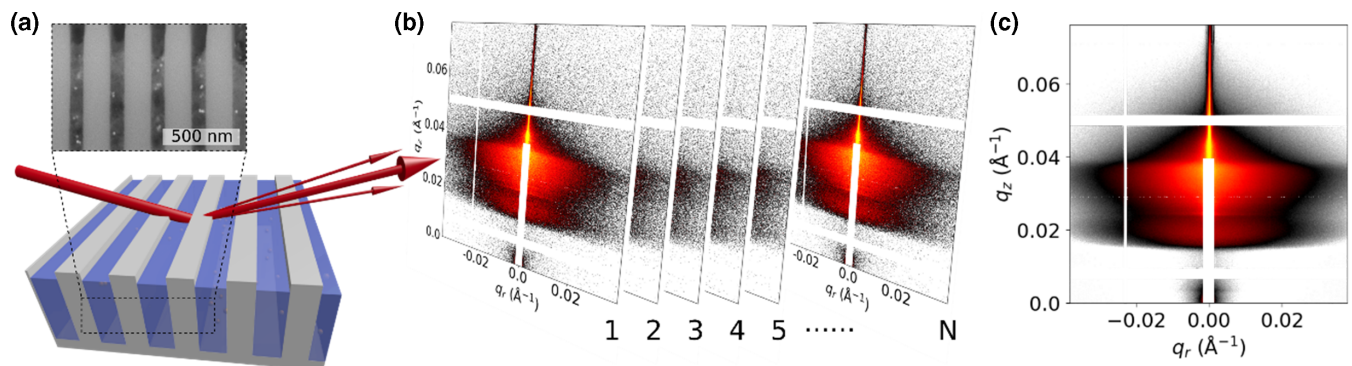


FIG. 2. (a) Schematic of grazing-incidence x-ray photon correlation spectroscopy (GI-XPCS) measurement of a nanograting filled with PEO and gold nanoparticles. (Inset) High-magnification SEM cross-sectional view of PEO confined within grating channels. Gold nanoparticles (AuNPs) are homogeneously dispersed within the nanoconfined PEO. (b) A series of x-ray detector images captured from one measurement at a single sample spot. The time sequence of scattering images provides information on the dynamics of nanoparticle motion. (c) A SAXS image from nanoconfined material, averaged over time and space (20 repeated measurements at separated sample spots; exposure time at each spot was 200 ms). The time-averaged image shows scattering from the substrate and the form factor of the spherical nanoparticles. We define q_z as the out-of-plane direction and q_r as the in-plane direction (gratings were measured with the beam across the grating grooves, as shown).

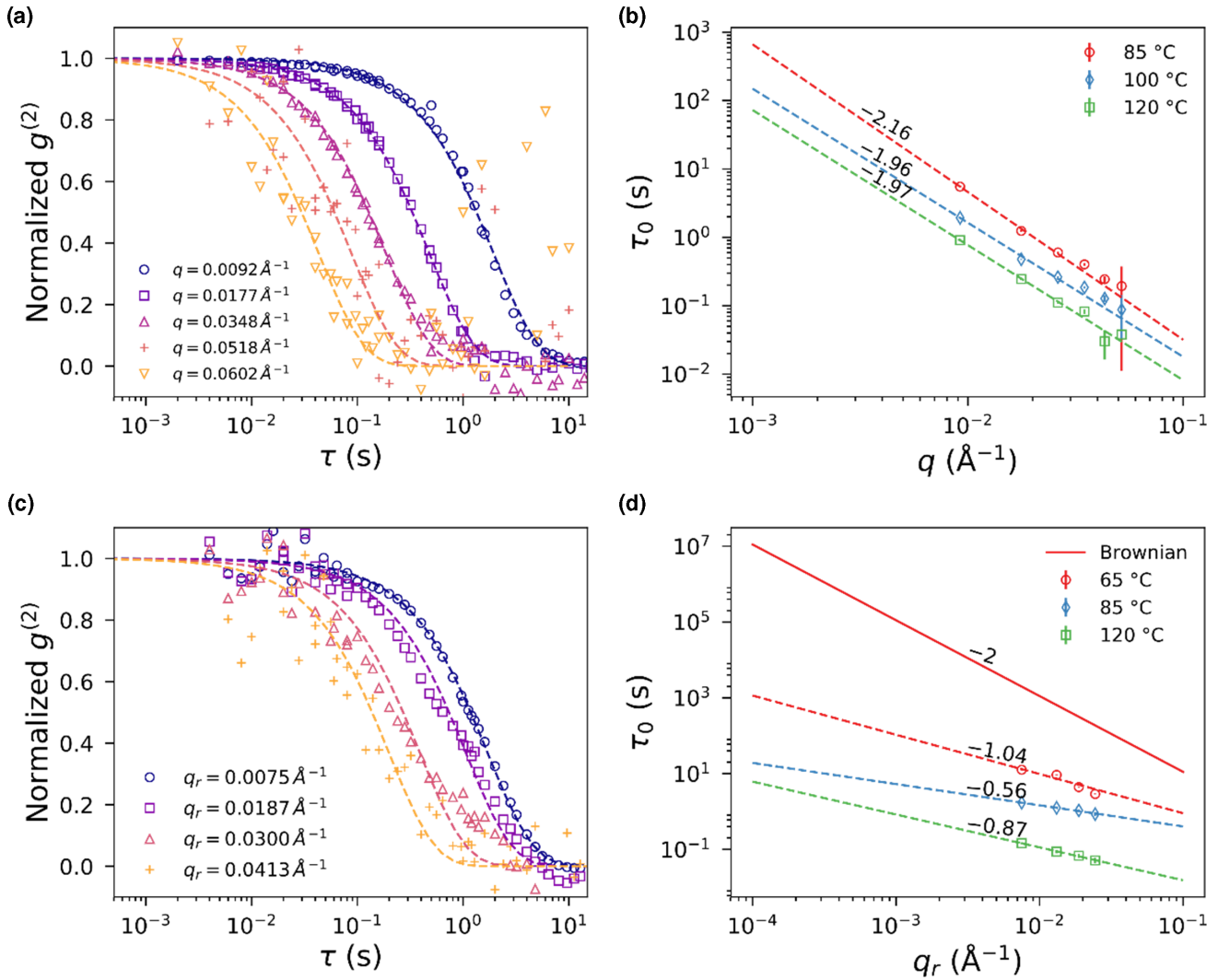


FIG. 3. (a),(b) GT-XPCS measurements (20 nm diameter AuNP probes): (a) normalized $g^{(2)}$ at different q for bulk PEO39k at 85 °C; (b) temperature-dependent time constants for bulk PEO39k versus q . (c),(d) GI-XPCS measurements: (c) normalized $g^{(2)}$ at different q_r (fixed $q_z = 0.0335 \text{ \AA}^{-1}$) for a bulk (dropcast) PEO39k film at 85 °C; (d) time constants for PEO39k versus q_r . The dashed lines in (a) and (c) are single exponential fits. In (b) and (d), the number on top of each line is the slope of a linear fit in the log-log graph (exponent of the power-law q dependence). The transmission scattering (GT) measurements exhibit the expected single exponential relaxation and a scaling of $\tau_0 \sim q^{-2}$, indicative of Brownian motion of the nanoparticle tracers. The corresponding grazing-incidence (GI) measurements instead exhibit slightly stretched exponential behavior, and a different scaling. These small discrepancies can be attributed to the GI measurement geometry. Importantly, the magnitude and trends in τ_0 are correctly probed in GI geometry (up to a systematic error).

of 0.24° (the critical angle for PEO is $\sim 0.13^\circ$ at 9.65 keV) and collected a time series where the total x-ray dose at any sample position was below the experimentally measured damage threshold [Fig. 2(b)].

Measurements of a bulk PEO sample using GI-XPCS yield a melt viscosity consistent with previous reports, validating the experimental approach. Figure 3 shows XPCS data for $\sim 1 \mu\text{m}$ thick dropcast film of PEO (molecular weight $M_w = 39 \text{ kg/mol}$), comparing conventional transmission scattering with grazing-incidence scattering. For transmission measurements, we used the grazing-transmission SAXS geometry (GTSAXS) [41], wherein the x-ray beam is directed to the downstream *edge* of the sample at an incident angle larger

than the critical angle, thus avoiding multiple scattering processes that can affect GISAXS measurements. We compute a temporal correlation curve ($g^{(2)}$) by selecting a particular region of interest (ROI) on the detector and computing the average correlation for a range of temporal intervals (τ) [42,43]. For the grazing transmission-geometry (GT-XPCS) measurements, we combine data over rings of constant q to improve signal-to-noise. However, for grazing-incidence experiments (GI-XPCS), we select ROIs over a limited range of q_r and q_z , due to the multiple scattering effect from the reflection geometry [44–47].

We systematically vary q by choosing a series of equally spaced ROIs (Fig. S3). The $g^{(2)}$ curves at different q values

are fit to an exponential decay function,

$$g^{(2)} = \beta e^{-\frac{t}{\tau_0}} + g_\infty, \quad (1)$$

where β is the Siegert factor [38], g_∞ is the lower plateau, and τ_0 is the characteristic time constant. $g^{(2)}$ is normalized to a range between 0 and 1 [Fig. 3(a)] by

$$g'^{(2)} = (g^{(2)} - g_\infty)/\beta = e^{-\frac{t}{\tau_0}}, \quad (2)$$

where $g'^{(2)}$ is the normalized $g^{(2)}$. The autocorrelation functions gradually shift to the right (slower dynamics) as q decreases. This is expected since longer diffusion times (slower dynamics) are associated with larger distances in real space (smaller q in the reciprocal space).

For simple Brownian motion, the relationship between the time constant (τ_0) and q can be derived from the three-dimensional form of Fick's Law. Assuming the AuNPs undergo Brownian motion in all directions, their mean-square displacement ($\langle \Delta x^2 \rangle$) obeys the relationship

$$\Delta x^2 = 6D_0\tau_0, \quad (3)$$

where D_0 is the diffusion coefficient. In reciprocal space, this is equivalent to

$$D_0\tau_0 = q^{-2}. \quad (4)$$

Our GT-XPCS measurements of a thick PEO film [Fig. 3(a)], PEO39k, are consistent with Eq. (4), with τ_0 proportional to $1/q^2$ (i.e., a slope of -2 on a log-log scale). We convert the measured diffusion coefficient into an effective viscosity, using the Stokes-Einstein equation:

$$\eta = \frac{k_B T}{6\pi D_0 r}, \quad (5)$$

where k_B is Boltzmann's constant, T is the absolute temperature, and r is the AuNP radius.

Our GT-XPCS measurements of PEO39k at 85 °C yield a viscosity of ~ 700 Pa·s. Measurements at higher temperature show higher particle mobility (smaller τ_0), as expected, since the AuNP dynamics are determined by the viscosity of the confining medium (Fig. S5). Moreover, we find that the viscosity-temperature scaling measured by GT-XPCS is consistent with literature [48,49], confirming that measuring the motion of AuNP tracers is an effective probe of the viscoelastic response of the complex fluid.

In this experiment, we specifically chose AuNP diameters (10 nm or 20 nm) which are sufficiently large to ensure Stokes-Einstein scaling. Cai *et al.* [50,51] theoretically considered the diffusive behavior of nanoparticles of different sizes in entangled polymers, showing that the particle size relative to the polymer chain dimension dictates the particle's diffusive behavior. In particular, the diffusivity of a particle that is several times larger than chain dimensions of the polymer should follow the usual Stokes-Einstein prediction. Using fluctuation correlation spectroscopy, Grabowski *et al.* [52] reported Stokes-Einstein scaling for particles whose diameter are 5 times larger than the mesh size d_t (a metric for the chain dimensions as defined by the average spacing between polymer chain entanglements), $2r/d_t > 5$. We calculate [53] for PEO39k that $d_t = 3.7$ nm, and thus the AuNPs are >5 times the mesh size ($2r/d_t = 5.4$).

In order to obtain sufficient signal-to-noise in XPCS measurements of thin layers of nanoconfined material, we exploit the grazing-incidence geometry, which introduces artifacts that must be accounted for in the XPCS analysis. First, the q_z direction is distorted by refraction as the beam enters and exits the film [44–47]. Moreover, every detector pixel at a nominal q_z has two true q_z values associated with it, owing to scattering from both the direct beam and reflected beam. Thus, the temporal decorrelation measured for any ROI on the detector is in fact the mixture of two different decorrelations with slightly different time constants (owing to the slightly different q of the two contributions). Despite this complication, the results from GI geometry can be validated and interpreted [Fig. 3(b)]. We analyze the GI-XPCS data by using ROIs over a small span of q_r and q_z in the detector images, selected such that the competing q_z trends roughly cancel, and the q dependence is nearly entirely captured by q_r (Fig. S6 confirms that τ_0 is thereby nearly invariant as a function of q_z). The correlation curves measured in GI are found to be slightly stretched exponentials, which we attribute to the mixing of multiple correlation curves (refer to Fig. S7 for a quantitative analysis of this effect). This apparent stretching due to GI distortion would mask stretching of the decorrelation curve for physical reasons, such as a distribution of dynamic timescales. Thus, we fit the GI-XPCS data with a single exponential to extract a single characteristic time constant τ_0 . The q dependence of the GI data deviates from the -2 slope observed in the GT experimental geometry. The direct comparison between GT and GI data (Fig. 3) highlights the complicating effect of the GI geometry. However, this comparison also allows us to verify that the τ_0 obtained using our procedure is a valid measure of the system's effective viscosity (within a small systematic error).

AuNPs moving within PEO confined within nanogratings decorrelate significantly slower than in a bulk PEO39k film (Fig. 4); that is, the nanoparticles experience a higher effective viscosity in the nanoconfined geometry. Whereas AuNPs in bulk PEO39k decorrelate in approximately $\tau_0 \approx 2$ s (for $q_r = 0.00728 \text{ \AA}^{-1}$), the same AuNPs moving in the same PEO when confined to nanoscale volumes require much longer timescales to decorrelate ($\tau_0 \approx 1000$ s), demonstrating that the effective nanoscale viscosity of PEO under confinement is more than two orders of magnitude greater. This more than 500 times increase in rheological response compared to the bulk (Fig. 4) was observed for confinement along two dimensions (nanogratings; i.e., 1D nanovolumes) and also for confinement in all three dimensions (nanopores; i.e., 0D nanovolumes). A comparison is provided in Fig. S9. It is likely that the diffusive behavior of the nanoparticles under confinement is non-Brownian, which would lead to stretching of the decorrelation exponential. Indeed the measured correlation curves are not strictly exponential decays. However, given the GI distortion effect described above, it is not possible to robustly quantify the contribution to stretching that is “intrinsic,” that is, due to physical effects. In order to approximately determine the effective nanoscale viscosity experienced by the nanoparticles, we can nevertheless use the Stokes-Einstein equation, from which we estimate a viscosity of ~ 0.6 MPa·s under nanoconfinement.

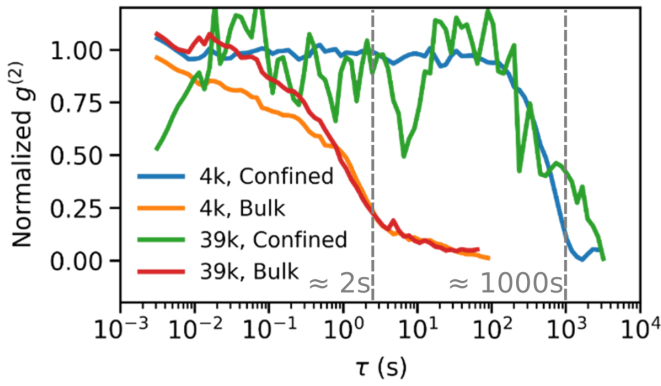


FIG. 4. Normalized $g^{(2)}$ at $(q_r = 0.00728 \text{ \AA}^{-1}, q_z = 0.0335 \text{ \AA}^{-1})$ of line grating filled with PEO4k (blue), bulk PEO4k (yellow), line grating filled with PEO39k (green), and bulk PEO39k (red), all measured in the GI geometry using 10 nm diameter AuNP probes. For both molecular weights, the bulk at this q exhibits relatively fast dynamics (with a relaxation time of ~ 2 s), whereas confinement drastically slows dynamics (higher viscosity). Confined materials were measured with the x-ray beam across the grating grooves, such that the in-plane (q_r) scattering probes AuNP motion along the long direction of the grating trenches.

Because these XPCS measurements are actually probing the statistical motion of the dispersed AuNPs, it is natural to wonder whether the observed dynamics represent a faithful report of the local hydrodynamic environment. For example, the spatial restrictions caused by nanoconfinement will modify the statistical measure of decorrelation, even with the matrix viscosity unchanged, because the AuNPs are more constrained in their diffusion directions. However, this effect only introduces an offset to the correlation curve (i.e., a nonzero baseline), stemming from the AuNPs' inability to diffuse arbitrarily far from their starting positions (and thus fully decorrelate; Fig. S8). Moreover such effects would be expected to be significant for measurements with the x-ray beam along the grating grooves, whereas we instead measure with the beam orthogonal to the grooves and are thus measuring the particle diffusion along the long direction of the grating trenches. It is also possible that AuNP motion is arrested due to binding to the confining volume sidewalls. SEM analysis of the confined materials both before and after thermal cycling showed AuNPs well dispersed within the PEO and not preferentially adhered to the side walls. Moreover, the eventual decay of $g^{(2)}$ confirms that the nanoparticles are not completely immobile. Intermittent sticking of nanoparticles to sidewalls is also possible and would influence average measured dynamics. However, in such a case one would observe two decorrelation times: one associated with intrinsic particle motion, and one associated with the timescale of particle binding and unbinding. We do not observe this experimentally. We also note that assuming the particles diffuse as in the bulk, the AuNPs would encounter sidewalls over timescales of ~ 4 s (approximate time for AuNPs to traverse 50 nm). Our measurements show a substantial shift of the correlation curve at timescales as short as 0.1 s (Fig. 4)—well before the AuNPs would (statistically) encounter a sidewall. Nanoparticle dimerization or aggregation would of course influence dynamics

measurements. The recovery of the expected viscosity of PEO when measuring in the bulk suggests that the dynamics measured by XPCS and analyzed assuming isolated particles is reasonable in this case. As with particle-sidewall interactions, we note that a population of aggregated particles would tend to have much slower dynamics. From the form factor measured in SAXS and the available SEM images, we conclude that there is a population of free particles, which would then be responsible for the shortest decorrelation time measured by XPCS (i.e., the dynamic timescales reported herein). It is of course difficult to disentangle the contributions of intrinsic shifts of the melt viscosity and collective phenomena between the AuNPs, the confinement walls, and the polymer network (which mediates interactions). We can nevertheless conclude that the dynamics measured by this approach is representative of the effective viscosity experienced by nanoscale objects moving in the complex fluid.

Complex fluids, such as polymers, have physical and mechanical properties that are scale-dependent. For example, polymer dynamics can be vastly different at the scale of the monomer, the chain, the network, and the continuum. Our measurements are probing the effective nanoscale viscosity of PEO when in close proximity to multiple interfaces. The confinement size of the gratings is ~ 100 nm; however, we note that for 20 nm diameter AuNP probes, the confinement size is perhaps better thought of as ~ 40 nm (the distance from the grating sidewall to the particle surface when the particle is centered in the grating). This can be compared to the polymer radius of gyration, which is $R_g = 6.7$ nm for PEO39k [54]. That is, we observe a dramatic effect of nanoscale confinement on the PEO dynamics and viscoelastic properties, even though the confinement size scale is $\sim 6R_g$, i.e., larger than the individual polymer chain dimensions. Our results can be compared to previous studies of the rheology of confined polymers. Granick and co-workers [25,55–57] studied the dynamic response of polyphenylmethylsiloxane confined between parallel plates, observing that the loss modulus increased by orders of magnitude as the thickness of the polymer sample decreased. These studies observed that the loss modulus scaled with the ratio of film thickness to the polymer radius of gyration [56]. The modulus was found to rise significantly when the film thickness dropped below $\sim 6R_g$, reaching a maximum value around $4R_g$, and finally decreasing as the film thickness dropped below $2R_g$. This effect was attributed to entanglement between neighboring polymer strands creating an effect akin to crosslinking. Luengo *et al.* [58] observed comparable effects in polybutadiene, with the effective viscosity increasing dramatically when the polymer was confined to a layer thickness approaching $6R_g$. Similar behavior is known for nanoparticles systems. Anderson and Zukoski [59] reported the behavior of silica nanoparticles in PEO melts of varying molecular weights and observed a dramatic increase in the viscosity of the composite material as the internanoparticle spacing approached small-integer multiples of the polymer radius of gyration. Moreover the enhancement was beyond what would be expected based on simple hydrodynamic arguments. These results can also be compared to shifts in the viscosity of small-molecule fluids when confined at molecular (~ 1 nm) scales. Extremely small confinement volumes (on the scale of the molecule) promote

ordered flow and thus extremely low effective viscosities (near-ballistic transport) [19,22,51]. Somewhat larger confinement volumes give rise to increased viscosity, depending on commensurability between the confinement and molecular dimensions [24–26]. Our results confirm that confinement effects in macromolecular systems extend far beyond the length scale of the individual “constituents”—whether one considers individual polymeric repeat-units or the overall polymer chain size—owing to the interchain entanglements. We experimentally confirm that polymers under nanoconfinement will exhibit an effective viscosity enhanced relative to the bulk. The viscous flow of a polymer is necessarily perturbed in proximity to interfaces. At the scale of individual chains, the finite size of the macromolecules as well as polymer-surface interactions will alter the effective viscosity. In the case of macromolecules, chain entanglements transmit this effect over further distances, leading to increased viscosity even when the confinement size scale is several times the radius of gyration.

IV. CONCLUSION

We have used grazing-incidence x-ray photon correlation spectroscopy to establish that a nanoconfined polymer melt exhibits an effective viscosity substantially larger than the same polymer melt when unconfined. Consistent with previous reports of polymers confined in thin films, the stiffening of the material occurs due to the proximity to interfaces, occurring at confinement sizes that are several times larger than the polymer chain dimensions. Tuning the polymer melt viscoelastic properties via confinement can be a vehicle

for enhancing the performance of nanocomposites or nanodevices. As one example, a nanoconfined ion-conducting polymer (such as PEO) may have beneficial properties for high-cyclability lithium metal rechargeable batteries, which require electrolytes with high mechanical stiffness to suppress the formation of deleterious dendrites [60–66].

ACKNOWLEDGMENTS

This research was carried out at the Center for Functional Nanomaterials and the National Synchrotron Light Source II, which are US DOE Office of Science Facilities, at Brookhaven National Laboratory under Contract No. DE-SC0012704. This work was partially supported by the Laboratory Directed Research and Development Program (LDRD) at Brookhaven National Laboratory.

Z.Z., B.M.O., A.F., L.W., K.G.Y., and C.T.B. designed the experiments; J.D. performed laser interference lithography exposure and development, under the supervision of C.-H.C. and F.T.F.; Y.T. and H.Z. prepared nanoparticle solutions; Z.Z. completed the bulk of the nanofabrication and sample preparation; Z.Z., B.M.O., K.G.Y., and J.L. performed XPCS measurements, with assistance from A.F., L.W., and Y.Z.; Y.Z. wrote the Python modules for analyzing XPCS data sets; M.K. and K.G.Y. performed simulations; Z.Z. performed numerical analysis and prepared figures, with feedback from B.M.O., A.F., L.W., K.G.Y., and C.T.B.; and Z.Z., B.O., M.K., K.G.Y. and C.T.B. wrote the manuscript. All authors commented on the manuscript.

The authors declare there are no conflicts of interest.

-
- [1] K. I. Winey and R. A. Vaia, *MRS Bull.* **32**, 314 (2007).
 - [2] K. M. Coakley, B. S. Srinivasan, J. M. Ziebarth, C. Goh, Y. Liu, and M. D. McGehee, *Adv. Funct. Mater.* **15**, 1927 (2005).
 - [3] Y. Yang, K. Mielczarek, M. Aryal, A. Zakhidov, and W. Hu, *Nanoscale* **6**, 7576 (2014).
 - [4] D. E. Johnston, K. G. Yager, C.-Y. Nam, B. M. Ocko, and C. T. Black, *Nano Lett.* **12**, 4181 (2012).
 - [5] S. H. Anastasiadis, K. Karatasos, G. Vlachos, E. Manias, and E. P. Giannelis, *Phys. Rev. Lett.* **84**, 915 (2000).
 - [6] M. K. Mundra, S. K. Donthu, V. P. Dravid, and J. M. Torkelson, *Nano Lett.* **7**, 713 (2007).
 - [7] J. A. Forrest, K. Dalnoki-Veress, J. R. Stevens, and J. R. Dutcher, *Phys. Rev. Lett.* **77**, 2002 (1996).
 - [8] S. Alexandris, P. Papadopoulos, G. Sakellariou, M. Steinhart, H.-J. Butt, and G. Floudas, *Macromolecules* **49**, 7400 (2016).
 - [9] R. M. Michell and A. J. Müller, *Prog. Polym. Sci.* **54-55**, 183 (2016).
 - [10] L. M. Cox, J. P. Killgore, Z. Li, Z. Zhang, D. C. Hurley, J. Xiao, and Y. Ding, *Adv. Mater.* **26**, 899 (2014).
 - [11] L. M. Cox, J. P. Killgore, Z. Li, R. Long, A. W. Sanders, J. Xiao, and Y. Ding, *Langmuir* **32**, 3691 (2016).
 - [12] Z. Zhang, L. Wang, and Y. Ding, *Langmuir* **29**, 3073 (2013).
 - [13] Y. Son, N. S. Martys, J. G. Hagedorn, and K. B. Migler, *Macromolecules* **36**, 5825 (2003).
 - [14] X.-C. Chen, H.-M. Li, F. Fang, Y.-W. Wu, M. Wang, G.-B. Ma, Y.-Q. Ma, D.-J. Shu, and R.-W. Peng, *Adv. Mater.* **24**, 2637 (2012).
 - [15] Z. Zhang, Z. Wang, and Y. Ding, *Polymer* **55**, 4150 (2014).
 - [16] J.-H. Lee, J. Y. Chung, and C. M. Stafford, *ACS Macro Lett.* **1**, 122 (2012).
 - [17] A. Azari and K. K. Müller-Nedebock, *Europhys. Lett.* **110**, 68004 (2015).
 - [18] H. D. Rowland, W. P. King, J. B. Pethica, and G. L. W. Cross, *Science* **322**, 720 (2008).
 - [19] D. M. Sussman, W.-S. Tung, K. I. Winey, K. S. Schweizer, and R. A. Riggleman, *Macromolecules* **47**, 6462 (2014).
 - [20] S. B. Darling, *Prog. Polym. Sci.* **32**, 1152 (2007).
 - [21] T.-S. Kim and R. H. Dauskardt, *Nano Lett.* **10**, 1955 (2010).
 - [22] W.-S. Tung, R. J. Composto, R. A. Riggleman, and K. I. Winey, *Macromolecules* **48**, 2324 (2015).
 - [23] K. Shin, S. Obukhov, J.-T. Chen, J. Huh, Y. Hwang, S. Mok, P. Dobryial, P. Thiyagarajan, and T. P. Russell, *Nat. Mater.* **6**, 961 (2007).
 - [24] K. A. Page, A. Kusoglu, C. M. Stafford, S. Kim, R. J. Kline, and A. Z. Weber, *Nano Lett.* **14**, 2299 (2014).
 - [25] H.-W. Hu and S. Granick, *Science* **258**, 1339 (1992).
 - [26] X. Li and G. B. McKenna, *Macromolecules* **48**, 6329 (2015).
 - [27] I. Wathuthanthri, W. Mao, and C.-H. Choi, *Opt. Lett.* **36**, 1593 (2011).

- [28] J. Ding, K. Du, I. Wathuthanthri, C.-H. Choi, F. T. Fisher, and E.-H. Yang, *J. Vacuum Sci. Tech. B* **32**, 06FF01 (2014).
- [29] X. Zhang, K. G. Yager, S. Kang, N. J. Fredin, B. Akgun, S. Satija, J. F. Douglas, A. Karim, and R. L. Jones, *Macromolecules* **43**, 1117 (2010).
- [30] Q. Peng, Y.-C. Tseng, S. B. Darling, and J. W. Elam, *Adv. Mater.* **22**, 5129 (2010).
- [31] A. Rahman, A. Ashraf, H. Xin, X. Tong, P. Sutter, M. D. Eisaman, and C. T. Black, *Nat. Commun.* **6**, 5963 (2015).
- [32] D. E. Johnston, M. Lu, and C. T. Black, *J. Micro/Nanolithogr/MEMS MOEMS* **11**, 031306 (2012).
- [33] See Supplemental Material at <http://link.aps.org/supplemental/10.1103/PhysRevE.100.062503> for additional electron microscopy images and details of the analysis.
- [34] A. Nogales and A. Fluerasu, *Eur. Polym. J.* **81**, 494 (2016).
- [35] T. Koga, C. Li, M. K. Endoh, J. Koo, M. Rafailovich, S. Narayanan, D. R. Lee, L. B. Lurio, and S. K. Sinha, *Phys. Rev. Lett.* **104**, 066101 (2010).
- [36] T. Koga and T. Kanaya, *Polymer* **105**, 339 (2016).
- [37] K. J. Alvine, Y. Dai, H. W. Ro, S. Narayanan, A. R. Sandy, C. L. Soles, and O. G. Shpyrko, *Phys. Rev. Lett.* **109**, 207801 (2012).
- [38] H. Guo, G. Bourret, R. B. Lennox, M. Sutton, J. L. Harden, and R. L. Leheny, *Phys. Rev. Lett.* **109**, 055901 (2012).
- [39] R. L. Leheny, M. C. Rogers, K. Chen, S. Narayanan, and J. L. Harden, *Curr. Opin. Colloid Interface Sci.* **20**, 261 (2015).
- [40] A. Papagiannopoulos, T. A. Waigh, A. Fluerasu, C. Fernyhough, and A. Madsen, *J. Phys.: Condensed Matter* **17**, L279 (2005).
- [41] X. Lu, K. G. Yager, D. Johnston, C. T. Black, and B. M. Ocko, *J. Appl. Crystallogr.* **46**, 165 (2013).
- [42] S. B. Dierker, R. Pindak, R. M. Fleming, I. K. Robinson, and L. Berman, *Phys. Rev. Lett.* **75**, 449 (1995).
- [43] D. M. Mills (ed.), *Third-Generation Hard X-Ray Synchrotron Radiation Sources: Source Properties, Optics, and Experimental Techniques* (Wiley-VCH, New York, NY, 2002).
- [44] P. Busch, M. Rauscher, D.-M. Smilgies, D. Posselt, and C. M. Papadakis, *J. Appl. Crystallogr.* **39**, 433 (2006).
- [45] B. Lee, I. Park, J. Yoon, S. Park, J. Kim, K.-W. Kim, T. Chang, and M. Ree, *Macromolecules* **38**, 4311 (2005).
- [46] R. Lazzari, F. Leroy, and G. Renaud, *Phys. Rev. B* **76**, 125411 (2007).
- [47] D. W. Breiby, O. Bunk, J. W. Andreasen, H. T. Lemke, and M. M. Nielsen, *J. Appl. Crystallogr.* **41**, 262 (2008).
- [48] M. Costagliola, R. Greco, and E. Martuscelli, *Polymer* **19**, 860 (1978).
- [49] A. Teramoto and H. Fujita, *Makromolekulare Chemie* **85**, 261 (1965).
- [50] L.-H. Cai, S. Panyukov, and M. Rubinstein, *Macromolecules* **44**, 7853 (2011).
- [51] L.-H. Cai, S. Panyukov, and M. Rubinstein, *Macromolecules* **48**, 847 (2015).
- [52] C. A. Grabowski and A. Mukhopadhyay, *Macromolecules* **47**, 7238 (2014).
- [53] J. E. Mark, *Polymer Data Handbook*, 2nd ed. (Oxford University Press, Oxford, 2009).
- [54] D. R. Beech and C. Booth, *J. Polymer Sci. A-2: Polymer Phys.* **7**, 575 (1969).
- [55] S. Granick and H.-W. Hu, *Langmuir* **10**, 3857 (1994).
- [56] S. Granick, H.-W. Hu, and G. A. Carson, *Langmuir* **10**, 3867 (1994).
- [57] J. Peanasky, L. L. Cai, S. Granick, and C. R. Kessel, *Langmuir* **10**, 3874 (1994).
- [58] G. Luengo, F.-J. Schmitt, R. Hill, and J. Israelachvili, *Macromolecules* **30**, 2482 (1997).
- [59] B. J. Anderson and C. F. Zukoski, *Macromolecules* **42**, 8370 (2009).
- [60] J. M. Tarascon and M. Armand, *Nature (London)* **414**, 359 (2001).
- [61] C. Monroe and J. Newman, *J. Electrochem. Soc.* **152**, A396 (2005).
- [62] R. Bouchet *et al.*, *Nat. Mater.* **12**, 452 (2013).
- [63] R. Khurana, J. L. Schaefer, L. A. Archer, and G. W. Coates, *J. Am. Chem. Soc.* **136**, 7395 (2014).
- [64] Q. Pan, D. M. Smith, H. Qi, S. Wang, and C. Y. Li, *Adv. Mater.* **27**, 5995 (2015).
- [65] Y. Lu, K. Korf, Y. Kambe, Z. Tu, and L. A. Archer, *Angew. Chem. Intl. Ed.* **53**, 488 (2014).
- [66] J. Zhang *et al.*, *Nano Lett.* **15**, 3398 (2015).